AIAA SciTech Forum
6-10 January 2025, Orlando, FL
AIAA SCITECH 2025 Forum

10.2514/6.2025-1446



# An Experimental Investigation of the Dynamic Icing Process on a Multirotor UAV Rotor in Forward Flight

Abdallah Samad[1], Anvesh Dhulipalla[2], Kayde Bowers[3], Justin Rodriguez[4] and Hui Hu[5]
*Department of Aerospace Engineering, Iowa State University, Ames, Iowa, 50011*

**An experimental study was conducted to characterize the dynamic ice accretion process on the rotating blades of UAVs in forward flight to document the ice shapes accreted on the blade surfaces as well as to evaluate the icing-induced detrimental effects. The experimental study was conducted in the unique Icing Research Tunnel available at Iowa State University (ISU-IRT) for a variety of different icing conditions (i.e., glaze, mixed and rime ice). Real-time measurements of the aerodynamic forces and motor power consumption were made to quantify the performance degradation under different icing regimes. Moreover, a "phase-locked" high-speed imaging technique was employed to reveal the instantaneous and key features of the ice accretion on the rotor blades. The collected data are used to deepen the understanding of underlying physics regarding the ice accretion process on rotating geometry and to generate a database of 2D & 3D ice shapes collected on the spinning rotor.**

## I. Introduction

The use of Unmanned Aerial Vehicles (UAVs) has recently become very well common and diversified across different recreational, economic and military activities [1]. Their small size and relatively inexpensive cost make them a viable product with many predictions of even more growth UAV markets worldwide [2]. Among the different UAV designs, most of them involve the use of at least one propeller or multiple rotors. Its ability to perform vertical take-offs and landings, hover in place, and provide exceptional maneuverability makes it the most commonly chosen propulsion mechanism for small UAVs. These features not only draw considerable interest but also broaden the range of UAV applications. As drone usage continues to grow, operations in cold environments are becoming more frequent. Consequently, icing on the propeller, a critical element of the propulsion system—has emerged as a key concern [3]. Rotary wing UAVs are particularly vulnerable to in-flight icing mainly due to the small size of the rotors, their high rotation speeds and also due to the fact that most UAVs operate at altitudes directly inside the icing envelope [4]. Icing is known to heavily increase the power consumption of the electric motors onboard of UAVs [5]. Documented evidence of multiple controlled experimental research studies shows the power consumption could increase by up to 300% when exposed to icing conditions for 2 or 3 minutes [6]. Moreover, icing changes the aerodynamic shape of the rotor airfoils and therefore directly increasing the drag and reducing the aerodynamic lift generated which could lead to up to 70% thrust loss according to a recent study [7].

In recent years, the subjects of rotor icing and the development of ice protection systems for rotor systems have gained significant traction with multiple research facilities exploring icing effects on rotor systems [8], [9], [10], [11]. Ice protection systems have been recently studied and explored in multiple different forms and mainly categorized as passive strategies including the use of icephobic or superhydrophobic coatings [12], [13], [14], [15], active strategies employing the use of blade-embedded heating elements [16], [17], [18], while hybrid strategies have also shown promise [19]. However, the underlying physics and modeling techniques are still interesting subjects of study since

[1] Postdoctoral Research Associate, Department of Aerospace Engineering.
[2] PhD Candidate, Department of Aerospace Engineering.
[3] PhD Candidate, Department of Aerospace Engineering.
[4] Undergraduate Student, Department of Mechanical Engineering.
[5] Anson Marston Distinguished Professor in Engineering, Dept. Aerospace Engineering, AIAA Associate Fellow, Email: huhui@iastate.edu.

further improvements in predictive models for heat and mass balance transfer are needed [20]. As rotary wing geometries fly through icing clouds, the small, supercooled liquid droplets impact the blade surfaces causing them to flow over the rotor blades and freeze [7]. The freezing could occur immediately or be delayed depending on the how quickly the latent heat of water fusion could be released [21]. This process is heavily dependent on the Liquid Water Content *LWC* and the freestream temperature of the surrounding air [22]. When the temperature is very low and the *LWC* is small, the droplets freeze immediately upon impact forming an opaque rime ice accumulation [23]. On the other hand, for larger *LWC*s and relatively warmer temperatures, glaze ice is formed which is characterized by its translucent color and complex ice shapes [24]. These ice structures would later heavily disrupt the flow behavior around the rotor blades, leading to changes in the aerodynamic behavior and structural vibrations [25]. While significant progress has been made in recent years in the area of UAV fixed wing/rotor icing [26], a significant effort is still needed to further develop more robust water and mass models for ice accretion on UAV airframes and components [27].

The objective of this paper is to conduct a comprehensive experimental campaign to analyze and document the ice accretion process on rotating UAV rotor blades. In this study, experiments are carried at the Iowa State University's Icing Research Tunnel (ISU-IRT) on a model UAV rotor for a wide range of icing conditions. Ice shapes were documented using a newly acquired 3D scanning system, providing both fully 3D digital models of the iced rotors as well as 2D cross sectional ice shapes across the blade radii. A high-speed imaging system was used to document the transient and instantaneous dynamic icing process over the rotor blade surfaces. In terms of data collection and measurements, the aerodynamic forces generated by the model rotor were measured using a highly sensitive force transducer whereas the motor power consumption was measured using a hall effect current sensor. The data collected in this research are meant to provide a deeper understanding of the icing process and its effects on UAV rotor operations. Finally, the high-quality ice shapes collected for a wide range of icing conditions could help other research groups develop and validate their numerical models of icing simulations on rotating geometries.

## II.Experimental Setup and Test Model

The ISU-IRT is leveraged for the present experimental study. As illustrated in Figure 1, The tunnel features a test section measuring 2.0 *m* in length, 0.4 *m* in width, and 0.4 *m* in height, with four transparent side walls. It is equipped to achieve a maximum wind speed of 60 *m/s* and an airflow temperature as low as -25°C. Positioned at the entrance of the contraction section are eight pneumatic atomizer/spray nozzles designed to introduce micro-sized water droplets (ranging from 10 to 100 $\mu m$). These droplets are effectively cooled to the air temperature during flight, in tandem with the airflow, before reaching the test model. The manipulation of water flow rates through the spray nozzles allows for adjustment of the liquid water content (*LWC*) within the ISU-IRT, ranging from 0.1 $g/m^3$ to 5.0 $g/m^3$. In summary, the ISU-IRT enables the simulation of atmospheric icing phenomena across various icing conditions, spanning from dry rime to wet glaze icing conditions. Additional details about the ISU-IRT can be found in Waldman & Hu [28].

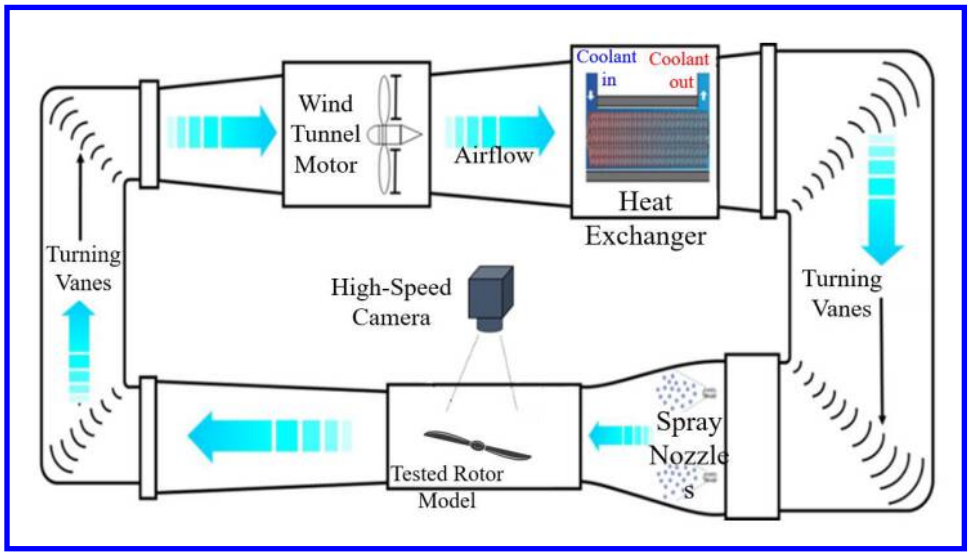


Figure 1 A Schematic of the Overall Test Setup used in this Study.

The test model used in the present study is a two-blade rotor with a radius $R = 127\ mm$, commonly used for UAV applications. The blades feature conventional airfoil cross-sections and platform profiles commonly utilized in rotor blade designs. The rotor blades are driven by an electric brushless DC motor (Scorpion SII-4035-380KV) that is paired with an 80 Amps Electronic Speed Controller (ESC). A DC power supply was used to provide a constant voltage of 16 $V$ to the motor. During the experiments, the rotation speed of the rotor blades was kept constant at 4000 rpm by using a PID controller. A wireless tachometer was used to monitor the real-time rotation speed of the rotor blades and to provide a digital pulse signal to the PID controller. Phase-locked images of the rotating blades during the experiments were acquired by coupling a high-speed camera to the digital pulse signal of the tachometer. The high-speed camera was placed above the rotation plane and images highlighting the instantaneous dynamic icing process over the blade surfaces were obtained. Moreover, a high-sensitive load cell (i.e., ATI, model F/T Sensor: mini45 IP65) was connected to the bottom of the test setup module to measure the aerodynamic forces generated by the rotor model under different test conditions. The current supplied to the electric motor during the experiments was measured real-time using a hall-effect current transducer to record any changes arising from the icing process or other external interferences.

In order to document the ice shapes obtained on the rotor blades at different icing times and conditions, a 3D scanning system was used to obtain fully 3D digitized models of the iced rotor blades. The 3D scanner used was the Artec Spider II. For all experiments presented in this work and after the test case was concluded, the rotor blades were transferred to a large cold chamber containing a custom-built rotating stand where the blades were fixed for scanning as shown in Figure 2. The iced rotor blades were spray painted with a very thin layer of opaque paint to make the transparent ice surfaces scannable.

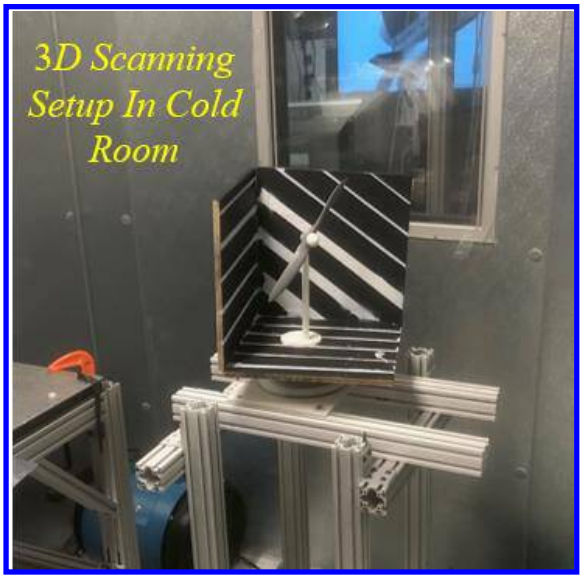


Figure 2 3D Scanning Test Stand Used in This Study

The experiments of this work and the documented ice shapes were done for a wide variety of icing conditions as shown in Table 1. The rotation speed of the blades was set constant at 4000 *rpm* whereas the tunnel's freestream velocity was set to 10 *m/s*. Tests at – 5 °C and – 10 °C were conducted for an LWC values of 1.00 $g/m^3$ whereas tests done at – 15 °C were done for three different LWC values of 0.50, 1.00 and 2.00 $g/m^3$. For all the aforementioned test cases, two repetitions were made with each having a different icing time. For the first test run, the icing time on the rotating blades was 60 seconds whereas in the second run, 120 seconds of icing were allowed. For all tests, the aerodynamic force measurements and motor power consumption data were recorded, high-speed images of the entire icing process were taken and at the end of each test, the rotor blades were 3D scanned.

Table 1 Operational and Icing Conditions Used for the Experiments of This Work

| $T_\infty$ (°C) | $LWC$ ($g/m^3$) | *Icing Time (s)* | Ω (RPM) | $V_\infty$ ($m/s$) | Advance Ratio | $MVD$ ($\mu m$) |
|---|---|---|---|---|---|---|
| − 5 | 1.00 | 60 | 4000 | 10 | 0.17 | 20-30 |
| | | 120 | | | | |
| − 10 | 1.00 | 60 | | | | |
| | | 120 | | | | |
| − 15 | 0.50 | 60 | | | | |
| | | 120 | | | | |
| | 1.00 | 60 | | | | |
| | | 120 | | | | |
| | 2.00 | 60 | | | | |
| | | 120 | | | | |



## III. Measurement Results and Discussions

### A. High-Speed Images of the Dynamic Icing Process on Rotor Blades

High-speed images of the dynamic icing process on the rotor blades were acquired during the experiments. Figure 3 shows snapshots of the icing process for the glaze icing condition (i.e., $T_\infty = -5$°C and $LWC = 1.00\ g/m^3$). As clearly shown in the figures, the ice accretion process develops with impacting supercooled droplets partially freezing on the leading edge of the blade. At this relatively warm temperature, the latent heat of fusion is slow to release, and the impacting droplets partially freeze with the remainder flowing to nearby locations [21]. The partial freezing of the water causes water films to flow in across the radius of the blade towards tip, as a result of being carried away by the centrifugal forces associated with the rotation motion of the blades. As the icing process continues, the rivulets freeze in needle shapes forming complex structures that are known to severely disrupt the flow around the blade, leading to a decreased aerodynamic performance. “Lobster-tail” ice structures can also be clearly seen extending away from the blade tip. It should also be noted that the majority ice forms near the leading edge, with ice being almost absent from the suction side surface of the rotor blade for the same reasons discussed earlier. Recalling that the velocity profile from hub to tip varies linearly because of the rotation of the blades, thinner ice accumulation is seen near the hub as compared to the blade tips. Since the collection efficiency of impacting water droplets is directly related to the local blade section velocity [29], the lowest amounts of water caught by the blades would be near the hub and the highest would be near the tips and thus explaining the apparently thicker ice accumulation near the tip of the blade. Moreover, near the end of the test, a small portion of the ice seemed to have detached from the tip of the blade as a result of ice shedding that is driven by the centrifugal forces of the rotating blades. Shedding occurs when the combination of aerodynamic and centrifugal forces acting on the ice structure overcome the ice adhesion strength to the blade surface [30]. While shedding events occur during the icing process, the continuous impingement of the droplets causes a new cycle of ice accumulation to start, with ice growing again as seen clearly in images of Figure 3.

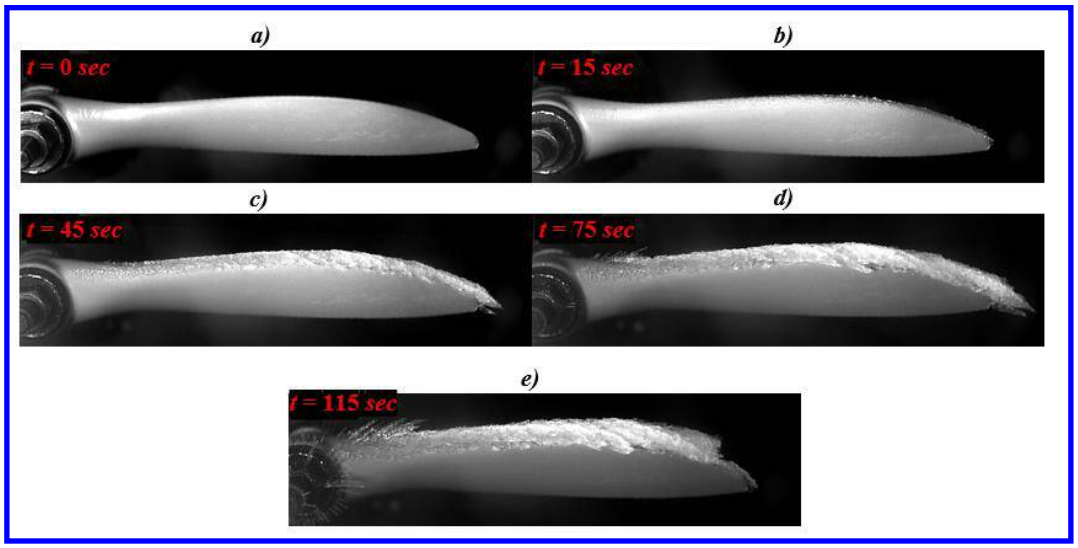


Figure 3 Snapshots of the Dynamic Icing Process over the Rotor Blades Surfaces for a Glaze Ice Test Condition

Figure 4 shows snapshots of the dynamic icing process over the blade surfaces for the test condition at the much colder temperature of $T_{\infty} = -15°C$. While the liquid water content was kept the same (i.e., $LWC = 1.00\ g/m^3$), the latent heat of fusion seemed to have released much more quickly compared to the glaze ice test condition since the accumulating ice in Figure 4 shows rime ice characteristics. The white and opaque nature of the ice seen in Figure 4 is a result of incoming water droplets freezing immediately upon impact, preventing any water rivulets to form or flow across the rotor surfaces [31]. As the icing process continues, the ice thickness grows almost normal to the leading edge with no apparent "lobster-tail" structures near the tip nor any "needles" forming anywhere else on the blade. Near the end of the test, a much larger ice shedding event can be clearly seen with ice detaching from more than half of the blade. Although ice shedding clears up the majority of the leading edge, it was also seen to leave some ice structures extending from below the leading edge, adding to the severe disruption of the flow around the rotor blades surfaces. Finally, and similar to what was explained before, a new ice layer would start accumulating over the area where the ice had shed as result of the continuous rotation of the blades as well as the continuous impacting water droplets originating from the icing wind tunnel nozzle array.

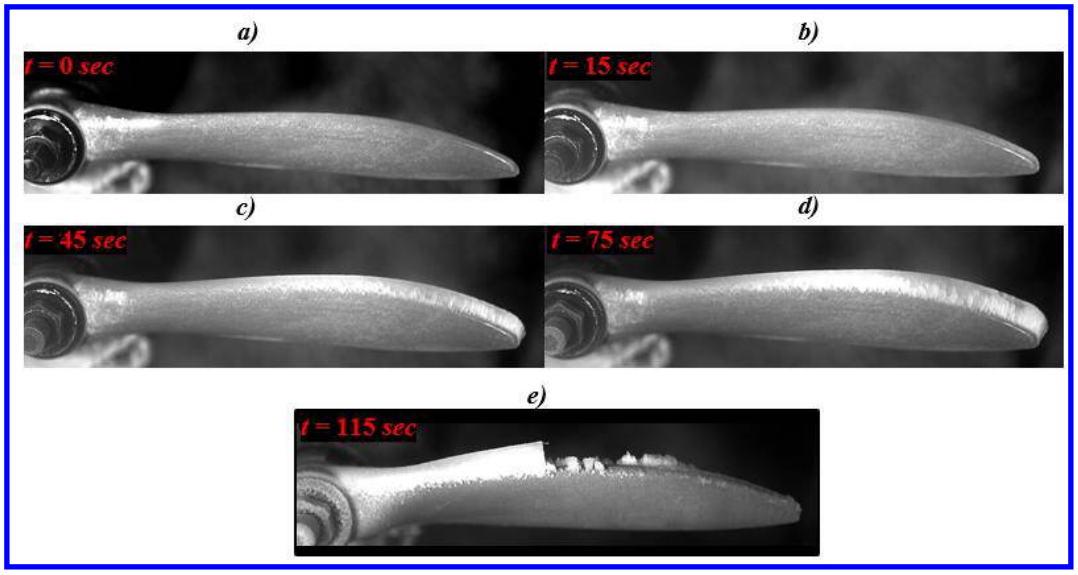


Figure 4: Snapshots of the Dynamic Icing Process over the Rotor Blades Surfaces for a Rime Ice Test Condition

To get a better outlook on the dynamic icing process over the rotating blades for the different icing conditions, the leading-edge ice thickness growth was monitored. Using the "phase-locked" high-speed imaging acquired during the experiments, and by using a calibrated image process technique to track the ice growth on the leading edge of the blades, the results of Figure 5 were obtained. Four different radial locations were selected (i.e., $r/R$ = 30, 50, 70 and 90%) where the ice growth versus time was monitored for two different icing conditions, the first being at $T_\infty = -5$°C and $LWC$ =1.00 $g/m^3$ while the other was at $T_\infty = -15$°C and $LWC$ = 1.00 $g/m^3$. For either condition, the ice thickness increases almost linearly versus time. Moreover, going from rotor hub to tip, the growth rate of ice was faster meaning that the ice accumulates and grows faster at $r/R$ = 90% compared to the other radial locations. The reason for that was directly attributed to the higher convective cooling occurring at the farther blade sections that are driven by the linearly increasing local blade velocity. The data in Figure 5 also clearly shows that the thickness obtained for the rime ice test case was larger compared to that of the glaze ice conditions. For rime ice, the immediate freezing of all the water droplets causes larger ice to build up to occur normal to the leading edge, whereas only partial freezing occurs for the glaze ice test case due to the latent heat of fusion not being totally released.

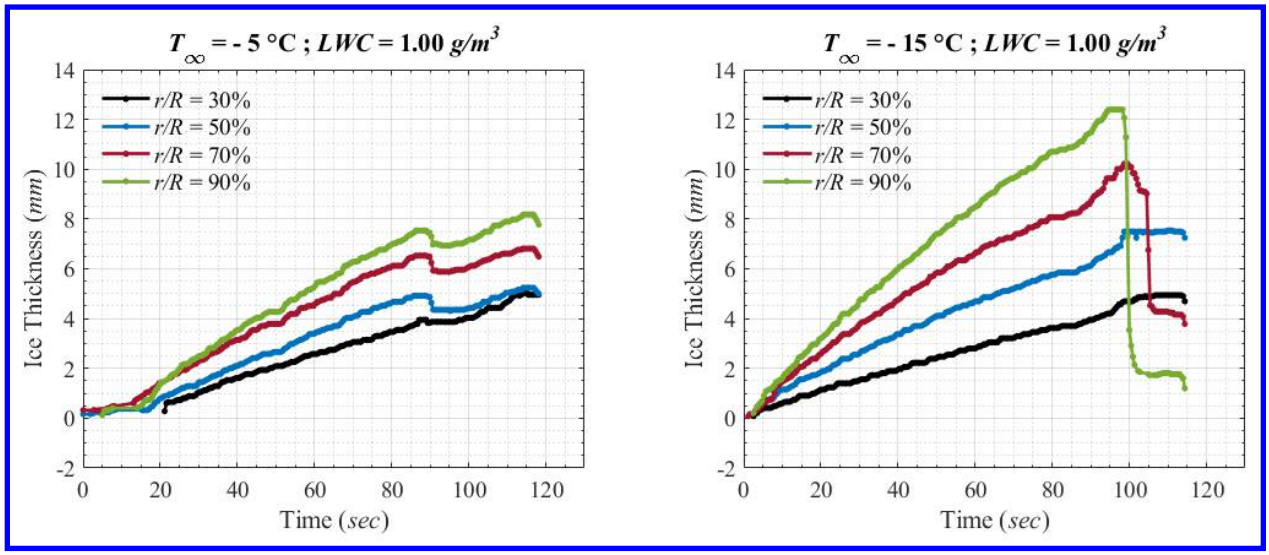


Figure 5: Growth of the ice thickness at the leading edge of the rotating blades for two selected cases: *a*) Glaze Ice and *b*) Rime Ice

### B. Ice Shapes Acquired for Different Air Temperatures

*1. Ice Shapes after 1 minute of icing experiment.*

As mentioned earlier, a newly acquired 3D scanning system by Iowa State University was used in the present work to document the 3D iced rotor blades' geometry after each experiment. After each test, the rotor blades were removed from the test stand and transported immediately to a nearby cold chamber where the 3D scanning process was completed similar to what was described earlier in [30]. A very thin layer of opaque paint was used to spray the ice structure over the rotor blades in order to overcome any translucency of ice that otherwise could not be scanned. Figure 6 shows the 3D iced blades geometries obtained through the 3D scanning of three different icing conditions at an $LWC$ = 1.00 $g/m^3$ as well as $T_\infty = -5, -10$ and $-15$°C, respectively. Moreover, the 3D scanned geometry of the "clean" and un-iced rotor blade is presented for comparison. Note that the 3D models presented in Figure 6 are for tests where the rotating blades were exposed to only 1 minute of icing before being stopped and scanned. As can be clearly seen in Figure 6, the general details of the ice shapes for all test cases were very well conserved and reflected in the 3D scans done in this work. For the tests at $T_\infty = -5$ and $-10$°C, the complex ice structures resulting from glaze ice accretions are obviously seen along with the "lobster-tail" ice shapes extending beyond the rotor blade tip section [32]. For the test case $-10$°C, a shedding event could be noticed to have occurred near the tip, with the ice shape being partially "discontinued" and a new layer of ice extending over it. On the other hand, no shedding events were noticed for the test cases at $-5$°C or $-15$°C during the 60 seconds of icing. For the test case at $-15$°C, the rime ice

accumulation can also be clearly distinguished since the ice structures grew normal to the leading edge with a much smoother and regular ice shape seen across the blade radius. It should also be noted that while the suction side of the rotor blades was almost free of any ice accumulation, except near the leading edge section of the blade, the pressure side of the blade was almost completely covered with ice for all presented test conditions of Figure 6, in accordance with previous results obtained similar endeavors [30].

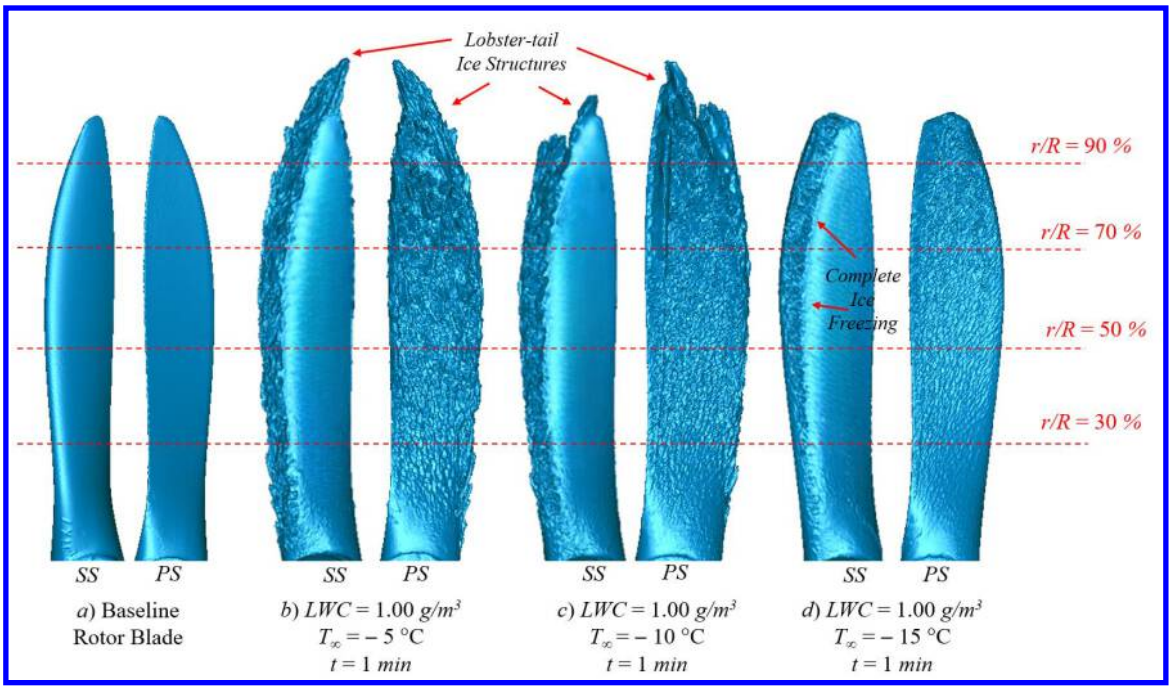


Figure 6. 3D Scanning Generated Models of the *a*) Baseline "Clean" Rotor Blades; as well as Following 1 Minute Icing Tests for the Test Conditions *b*) $T_\infty = -5$°C & $LWC = 1.00\ g/m^3$, *c*) $T_\infty = -10$°C & $LWC = 1.00\ g/m^3$ and *d*) $T_\infty = -15$°C & $LWC = 1.00\ g/m^3$

In order to obtain a clearer idea about the ice shapes and to better visualize the ice structures accumulated on the rotor surfaces for the test conditions of Figure 6, 2D cross sections of the ice shapes were made at four different locations across the blade radius. The cross sections were chosen at the nondimensional radial locations of $r/R$ = 30, 50, 70 and 90% of the blade. Figure 7 shows the acquired 2D ice shapes alongside the airfoil shapes of the clean blade for the different test conditions and radial locations. It should be noted that the blades used in this work had a high degree of twist between the hub and tip by design. Therefore, the ice shapes were rotated to lie almost horizontally with the leading edge of the clean rotor blades translated to the axes' origin for better visualization and for better assessment of the ice thickness.

As can be clearly seen in the ice shapes of Figure 7, the rime ice accretion (i.e., the test at $T_\infty = -15$°C) ice shapes mostly conformed to the original airfoil shape, adding thickness to the leading edge and pressure of the airfoils in a direction almost normal to the blade airfoils. However, the glaze ice accretions that were associated with the $T_\infty = -5$ and −10°C test conditions of this work showed complex ice shapes heights exceeding the original airfoil thicknesses of the clean rotor blades. Moreover, while the tests at relatively warmer temperatures showed evidence of partial freezing of impacting droplets (i.e., freezing fraction < 1), they also showed ice thicknesses almost equal to those of the rime ice test cases, where a freezing fraction ~= 1 and complete freezing of incoming droplets is expected [33]. The reason for the comparable thickness is thought to be unique to rotor blades and is mainly due to the unfrozen water's ability to flow over the leading edge towards the tip direction as a result of the rotor-exerted centrifugal forces.

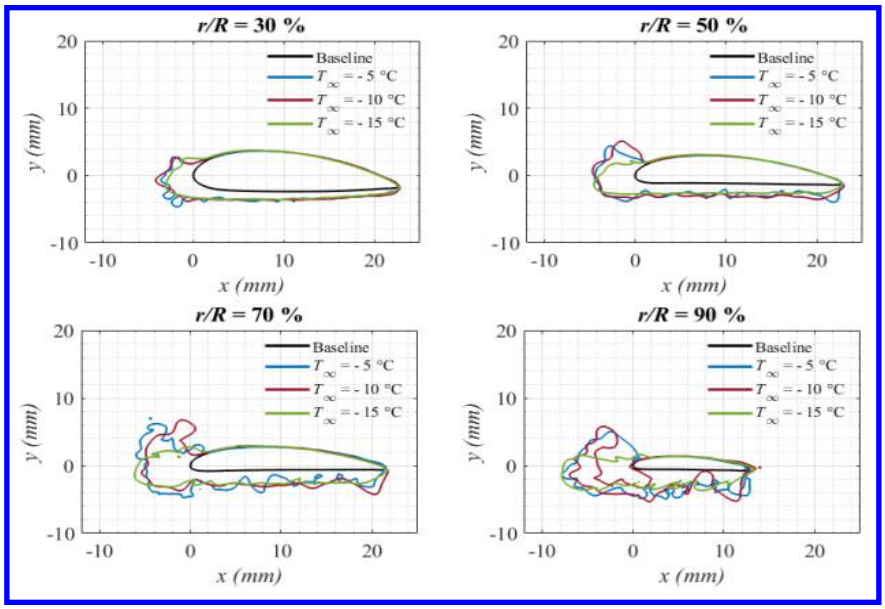


Figure 7. 2D Ice Shapes Collected Following Three 1 Minute Icing Test Cases at $T_\infty = -5, -10$ and $-15$°C and $LWC = 1.00\ g/m^3$

*2. Ice Shapes after 2 minutes of icing experiments.*

In a similar procedure to that presented earlier, 3D iced rotor blades' geometries following 2-miunte icing tests done at $T_\infty$ = -5°C, -10°C and $-15$°C are presented in Fig. 8. The 3D features of the ice shapes were also well preserved and reflected in the 3D models of Figure 8. For these tests with the longer icing time, the main distinction compared to the tests with shorter icing times was the pronounced evidence of ice shedding and re-accumulation. For the test case at $T_\infty$ = -5°C, a small shedding event could be noticed near the tip of the blade. On the other hand, a much larger and significant shedding could be seen to occur starting at $r/R$ = 50% of the test case at $T_\infty$ = -10°C as evidenced by the thicker ice found between the rotor hub and $r/R$ = 50%, followed by the thinner ice accumulation beyond the blade mid-span. The same description could also be attributed to shedding events for the test case at $T_\infty$ = -15°C.

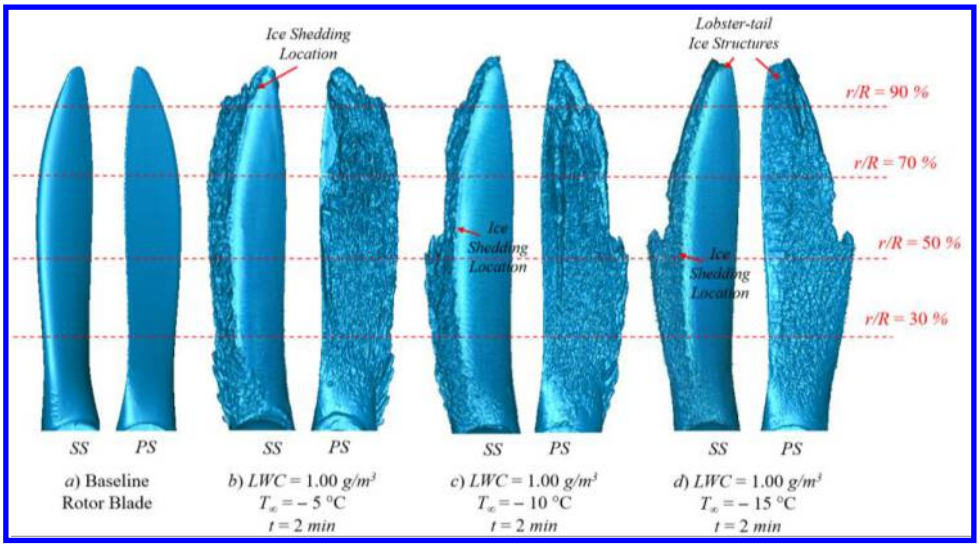


Figure 8 3D Scanning Generated Models of the *a*) Baseline "Clean" Rotor Blades; as well as Following 2 Minute Icing Tests for the Test Conditions *b*) $T_\infty = -5$°C & $LWC = 1.00\ g/m^3$, *c*) $T_\infty = -10$°C & $LWC = 1.00\ g/m^3$ and *d*) $T_\infty = -15$°C & $LWC = 1.00\ g/m^3$

As for the 2D cross sections of the ice shapes of the 3D scans presented earlier in Figure 8, Figure 9 offers an expanded discussion overt the icing process details seen earlier for the shorter duration icing tests of Figure 7. At *r/R* = 30 and 50% of the blade span, where no ice shedding occurred, the rime ice accretion continued to grow normal to the blade surfaces forming very thick ice shapes around the leading edge and pressure side of the blade. Accordingly, the tests at $T_\infty = -5$ and $-10$°C continued to show irregular and complex ice shapes growing thicker than the airfoil's original thickness. Beyond *r/R* = 50%, the ice shedding events seen for the test cases at $T_\infty = -10$ and $-15$°C caused a significant reduction of the ice thicknesses near the leading edge, with the test case at $T_\infty = -5$°C showing a much larger ice thickness at *r/R* = 70 and 90%.

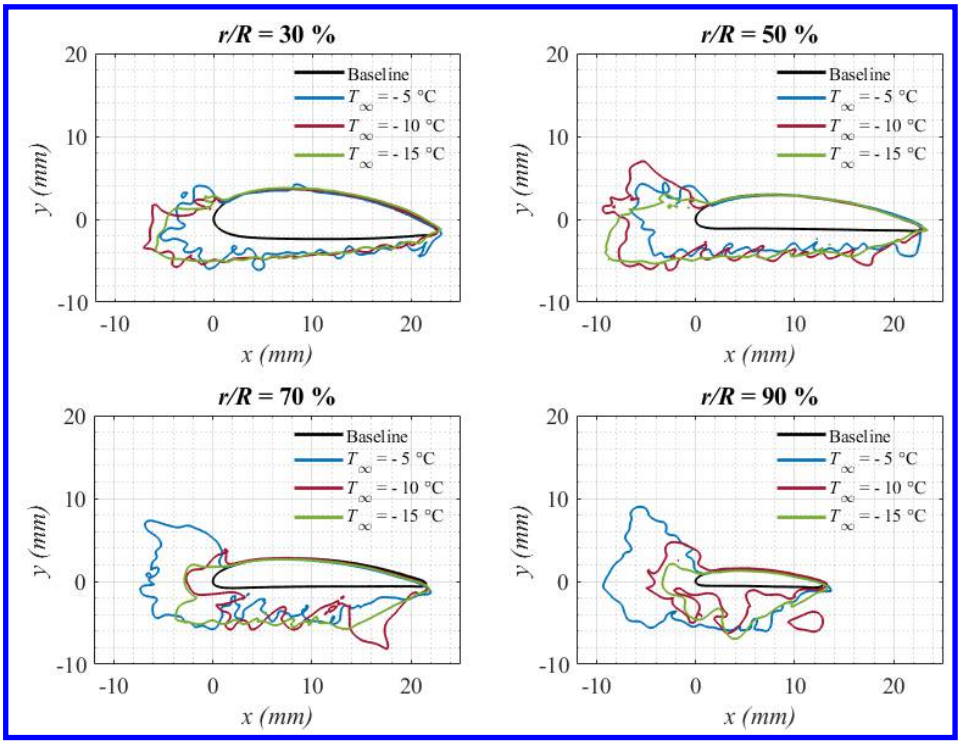


Figure 9. 2D Ice Shapes Collected Following Three 2 Minute Icing Test Cases at $T_\infty = -5, -10$ and $-15$°C and $LWC = 1.00$ $g/m^3$

### C. Ice Shapes Acquired for Different *LWC* - Rime Ice

*1. Ice Shapes after 1 minute of icing experiments.*

In this work, there was also an interest to investigate the effect of *LWC* on the ice shapes obtained on the rotor blades at very cold temperatures. Three test cases at $T_\infty = -15$°C were therefore done at three different liquid water contents (i.e., *LWC* = 0.50, 1.00 and 2.00 $g/m^3$). Figure 10 shows the 3D iced rotor geometries following the experiments with the tests at *LWC* = 0.50 and 1.00 $g/m^3$ showing similar ice accretions and with the typical rime ice accumulation. While the very low temperature has been earlier seen to be capable of withdrawing the entire latent heat of fusion from the impacting water droplets when the *LWC* value was 1.00 $g/m^3$, and while the test result of *LWC* = 0.50 $g/m^3$ shows similar a phenomenon, the results of Figure 10 show a different result when the *LWC* was further increased to 2.00 $g/m^3$. At the higher *LWC* value, a lot more impacting water droplets strike the surface and the resulting ice shape begins to carry more of mixed ice characteristics, with some of the droplets freezing immediately upon impacting, particularly aft of the leading edge, and others partially freezing and flowing over the rotor surface forming the unique "lobster-tail" over the blade tip area.

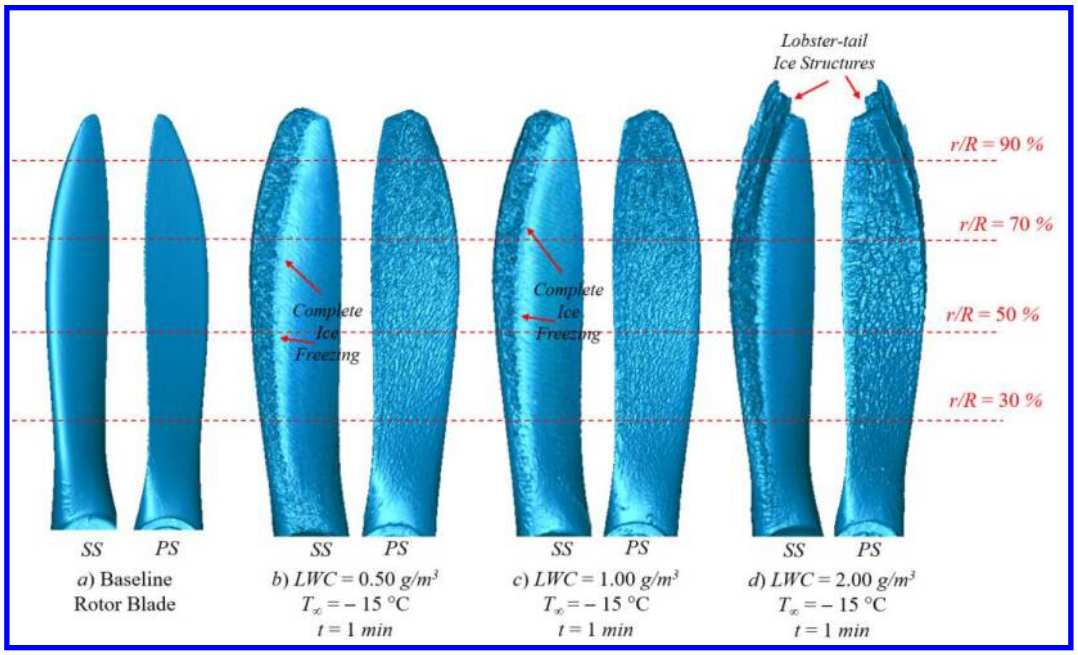


Figure 10 3D Scanning Generated Models of the *a*) Baseline "Clean" Rotor Blades; as well as Following 1 Minute Icing Tests for the Test Conditions *b*) $T_\infty = -15$°C & $LWC = 0.50\ g/m^3$, *c*) $T_\infty = -15$°C & $LWC = 1.00\ g/m^3$ and *d*) $T_\infty = -15$°C & $LWC = 2.00\ g/m^3$

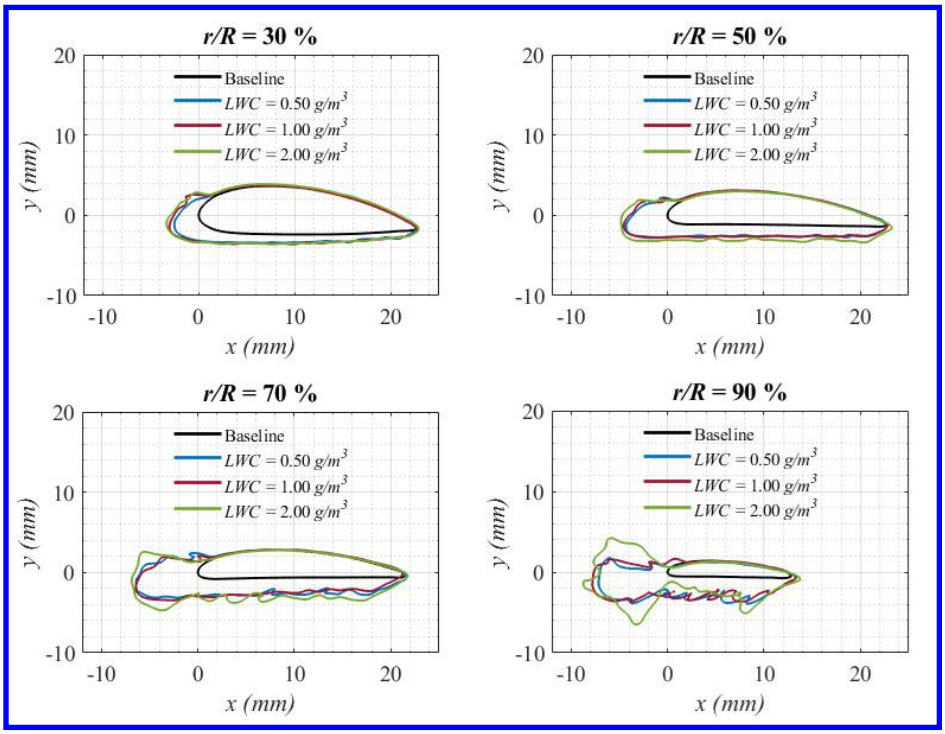


Figure 11 Ice Shapes Collected Following Three 1 Minute Icing Test Cases at $T_\infty = -15$°C and $LWC = 0.50$, 1.00 and 2.00 $g/m^3$

The effect of increased $LWC$ for the test cases at $T_\infty = -15$°C was also further examined by looking at the 2D cross sections of the ice shapes extracted from the 3D geometries of Figure 10. Figure 11 shows the 2D ice shapes taken at

*r/R* = 30, 50, 70 and 90% of the blade. While no significant effect of *LWC* could be noticed for the cross section locations at *r/R* = 50% or less, with the ice showing similar features and thicknesses around airfoil shape for all three *LWC*, a more pronounced distinction could be seen for the cross sections are *r/R* = 70 and 90% where the shapes acquired for *LWC* = 2.00 $g/m^3$ showing larger horn shapes extending in both the horizontal as well as the vertical directions, very similar to the glaze ice characteristics discussed earlier for tests with higher temperatures. As discussed earlier, at the beginning of the icing process for the test at the very cold temperature and relatively high *LWC*, the incoming droplets would freeze immediately upon impact but as the test progresses and the ice shape grows and collects even more water, the latent heat of fusion would not be removed entirely and the impacting water droplets start flowing towards the tip as a result of the rotor exerted centrifugal forces. For the tests at *LWC* = 0.50 and 1.00 $g/m^3$, the ice shapes closely resemble each other at all cross sections of the blade with almost equal thickness. For these lower values of *LWC*, the behavior indicates that the impingement limits of the incoming water droplets as well as the latent heat of fusion removal seem to be similar throughout the icing time of 60 seconds.

*2. Ice Shapes after 2 minutes of icing experiments.*

Figure 12 offers an expanded discussion of the previous test cases with 3D scans of the iced rotor blades after 2 minutes of icing exposure for $T_\infty = -15$°C and three different liquid water contents (i.e., *LWC* = 0.50, 1.00 and 2.00 $g/m^3$). The main distinction seen for these tests is clear evidence of large shedding events associated with the significant growth of ice thickness across the rotor blade that is overcome by the centrifugal forces exerted by the rotation motion of the blades. For the test case at *LWC* = 0.50 $g/m^3$, the ice accumulation after the ice shedding shows continued rime ice characteristics with ice growth normal to the leading edge. At the higher *LWC* of 1.00 $g/m^3$, an ice ridge could be seen forming starting from around *r/R* ~ 80% and slightly extending beyond the rotor tip. With the further increase of *LWC*, the "lobster-tail" grows beyond the rotor tip in a similar behavior to the one presented for the test with the shorter duration.

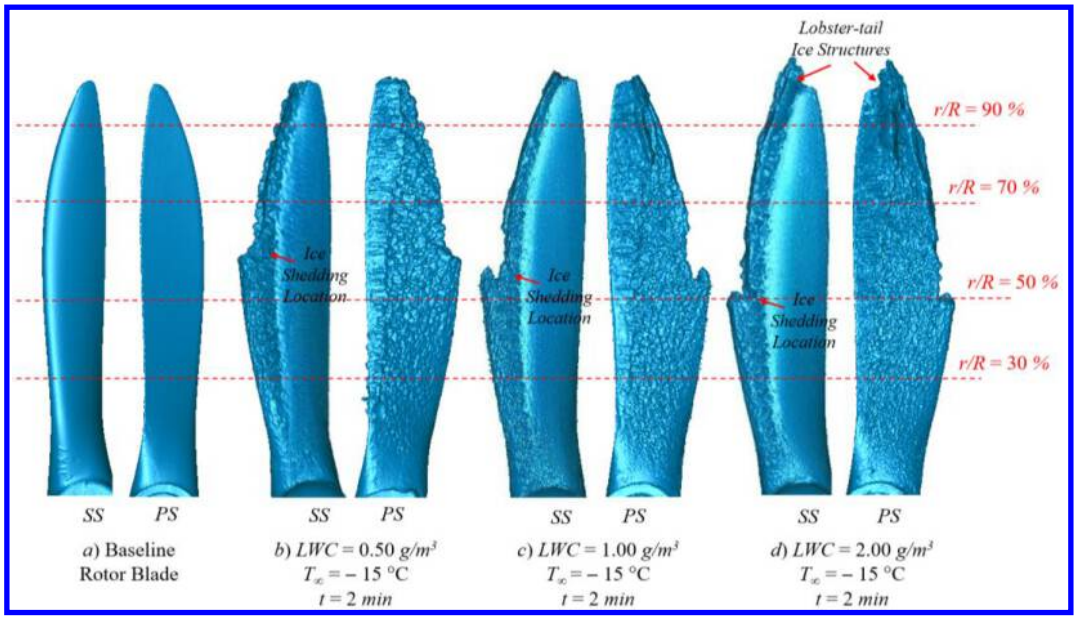


Figure 12. 3D Scanning Generated Models of the *a*) Baseline "Clean" Rotor Blades; as well as Following 2 Minute Icing Tests for the Test Conditions *b*) $T_\infty = -15$°C & *LWC* = 0.50 $g/m^3$, *c*) $T_\infty = -15$°C & *LWC* = 1.00 $g/m^3$ and *d*) $T_\infty = -15$°C & *LWC* = 2.00 $g/m^3$

The cross sectional 2D ice shapes of the 2-minute icing tests presented earlier in Figure 12 are shown in Figure 13. At *r/R* = 30%, the ice continued to grow in an almost similar shape and thickness for all three tested *LWC* values. A similar behavior is seen for the tests at *LWC* = 0.50 and 1.00 $g/m^3$ at *r/R* = 50% whereas a clear shedding event significantly reduced the ice shape for the test at *LWC* = 2.00 $g/m^3$. For the two further cross-sectional locations, ice shedding occurred for all three tested conditions, with the test at the highest *LWC* showing the largest ice shapes with the highest thicknesses as a result of the much higher water content and number of impacting water droplets on the blade surface.

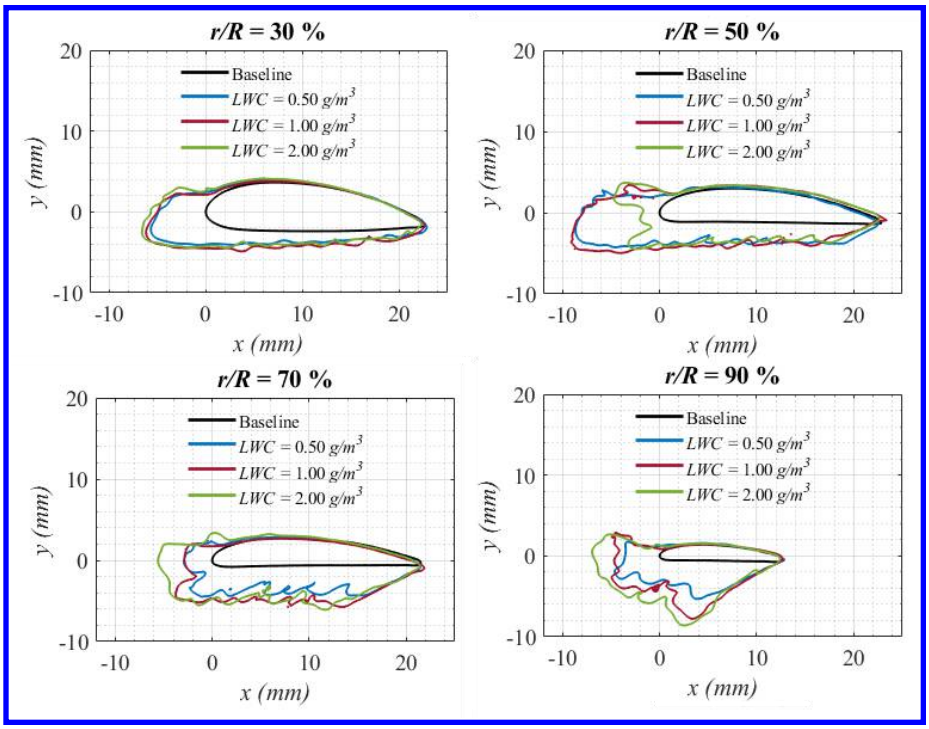


Figure 13 Ice Shapes Collected Following Three 2 Minute Icing Test Cases at $T_\infty = -15$°C and $LWC$ = 0.50, 1.00 and 2.00 $g/m^3$

### D. Lifting Force Characteristics and Aerodynamic Performance During the Dynamic Icing Process

In this work, the aerodynamic forces generated by the rotor model as well as the power supplied to the electric motor were recorded during all the conducted tests. Figure 14 shows the variation of the normalized thrust coefficient as well as the normalized power consumption of the motor during three different icing tests conducted at three different temperatures (i.e., $T_\infty = -5, -10$ & $-15$°C) and for an $LWC$ values of 1.00 $g/m^3$. In these plots, the rotor is allowed to spin at a constant rotation speed of 4000 rpm for 30 seconds before the icing spray is started at $t$ = 30 *sec*. As can be clearly seen in the figure, shortly after the icing spray is started, the thrust coefficient decreases, and the motor power consumption increases dramatically for all three test cases. For the power consumption, the tests at $T_\infty = -5$ and $-10$°C show a much more rapid increase of power consumption as compared to the test at $T_\infty = -15$°C which is mainly attributed to the complex ice shapes (i.e., "lobster-tail" ice shape and needle ice structures) attributed to glaze ice conditions that severely impact the flow around the blades and markedly increase the aerodynamic drag. While the test at the much colder temperature also shows a severe increase of power consumption, the slope of increase is lower mainly due to the impacting ice mostly conforming to the original airfoil shape, limiting the aerodynamic penalties associated with the growing ice shape. As for the thrust coefficient, the test at the colder temperature shows an overall more sever degradation of the thrust coefficient. It is thought that while the complex ice shapes generated by the glaze ice conditions severely increase the aerodynamic drag, they also tend to increase the rotor radius and possibly also extend the chord length which may result in added aerodynamic lift. With the complex ice shapes definitely lowering the original lift generated by the rotor blades alongside the increase of the effective rotor slightly adding to the lifting capacity of the rotor system, the decrease of thrust during the icing test was seen be more for the test at the much colder temperature.

Furthermore, ice shedding events would directly impact the aerodynamic forces and motor power consumption of the rotor system. The peaks in motor power consumption are directly related to ice shedding where the power consumption reduces abruptly after the ice is removed and quickly rises up again as a new layer of ice begins building up on the rotor surfaces. On the other hand, the sudden changes in thrust variation can also be directly at the same time instances of the ice shedding events. These sudden changes directly translate into instability of the UAV rotor performance, increased vibration rates and a higher risk of structural damage.

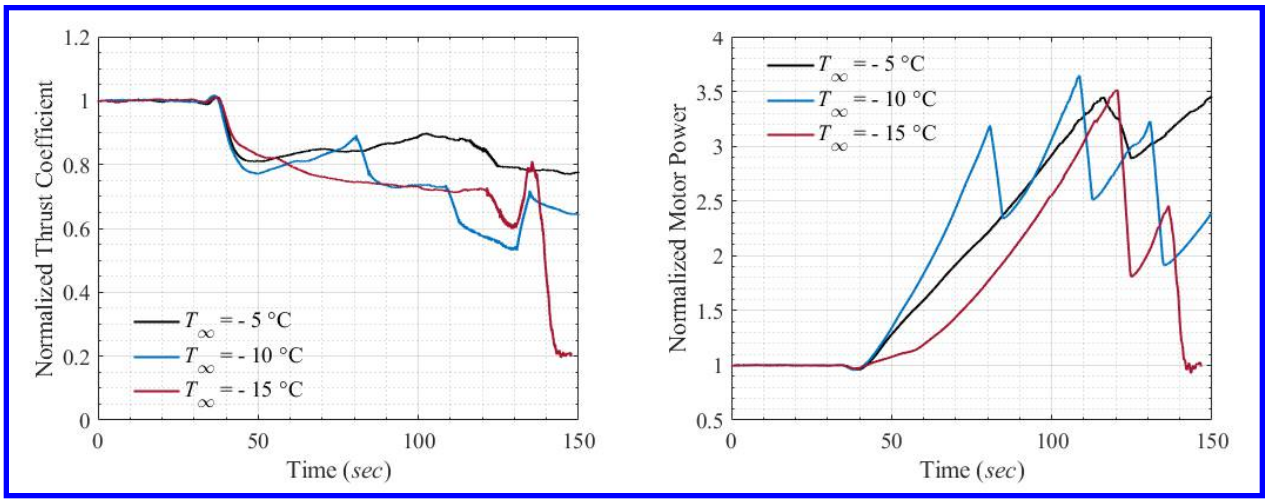


Figure 14 A Comparison of the Thrust Coefficient Variation and Motor Power Consumption Measured during Three Different Icing Tests at $T_\infty = -5, -10, \& -15$°C

## IV.Conclusion & Future Work

This paper presented experimental test cases conducted on a spinning rotor system in forward flight mode placed at the Iowa State University's Icing Research Tunnel. Experiments were conducted for a wide variety of icing conditions. Experimental data were collected and analyzed in terms of the high-seed imaging of the dynamic icing process, 3D scanning was performed on the iced rotor blades to document and investigate the 2D cross sectional ice shapes across the rotor radius and aerodynamic force measurements as well as motor power consumption were recorded. In this work, the dynamic icing process for the different icing conditions is discussed and ice shapes are analyzed. For future work, the data collected in this research will be used to further investigate scaling parameters along the iced rotor geometries and to further help in the development of heat and mass transfer balances for predictions of the icing process around rotating geometries.

## V. Funding Sources

The authors want to thank Robert Madore, Amrit Kumar, Harsha Sista, Kiran Digavalli, James Bension and Andrew Jordan of Iowa State University for their help in operating the ISU Icing Research Tunnel (ISU-IRT) Facility. The research is partially supported by the National Science Foundation (NSF) under the award numbers of CBET-1935363 and CBET- 2313310.

## VI. References

[1] M. Hassanalian and A. Abdelkefi, 'Classifications, applications, and design challenges of drones: A review', *Progress in Aerospace Sciences*, vol. 91, pp. 99–131, 2017, doi: https://doi.org/10.1016/j.paerosci.2017.04.003.

[2] B. Vergouw, H. Nagel, G. Bondt, and B. Custers, 'Drone technology: Types, payloads, applications, frequency spectrum issues and future developments', *The future of drone use: Opportunities and threats from ethical and legal perspectives*, pp. 21–45, 2016.

[3] M. Muhammed and M. S. Virk, 'Ice Accretion on Rotary-Wing Unmanned Aerial Vehicles—A Review Study', *Aerospace*, vol. 10, no. 3, p. 261, 2023, doi: https://doi.org/10.3390/aerospace10030261.

[4] Y. Cao, W. Tan, and Z. Wu, 'Aircraft icing: An ongoing threat to aviation safety', *Aerosp Sci Technol*, vol. 75, pp. 353–385, 2018, doi: https://doi.org/10.1016/j.ast.2017.12.028.

[5] M. Gao, C. H. Hugenholtz, T. A. Fox, M. Kucharczyk, T. E. Barchyn, and P. R. %J S. reports Nesbit, 'Weather constraints on global drone flyability', vol. 11, no. 1, p. 12092, 2021, doi: https://doi.org/10.1038/s41598-021-91325-w.

[6] Y. Liu, L. Li, W. Chen, W. Tian, and H. Hu, 'An experimental study on the aerodynamic performance degradation of a UAS propeller model induced by ice accretion process', *Exp Therm Fluid Sci*, vol. 102, pp. 101–112, Apr. 2019, doi: 10.1016/J.EXPTHERMFLUSCI.2018.11.008.

[7] E. Villeneuve, A. Samad, C. Volat, M. Béland, and M. Lapalme, 'Experimental Investigation of Icing Effects on a Hovering Drone Rotor Performance', *Drones*, vol. 6, no. 11, p. 345, 2022, doi: https://doi.org/10.3390/drones6110345.

[8] J. Burger, A. Scheicher, F. Knöbl, T. Neubauer, and V. Fill, '3D Reconstruction of Ice Shedding Trajectories on a Full-Scale Propeller Test Rig', *AIAA AVIATION FORUM AND ASCEND 2024*, Jul. 2024, doi: 10.2514/6.2024-4351.

[9] E. Villeneuve, A. Samad, C. Volat, M. Beland, and M. Lapalme, 'An Experimental Apparatus for Icing Tests of Low Altitude Hovering Drones', *Drones*, vol. 6, no. 3, p. 19, 2022, doi: https://doi.org/10.3390/drones6030068.

[10] J. R. Amon, R. Puffing, W. Hassler, D. Kozomara, S. Schweighart, and M. Gerstenbrand, 'Development of a Test Rig for Investigating Propeller and Rotor Icing', in *AIAA AVIATION FORUM AND ASCEND 2024*, Reston, Virginia: American Institute of Aeronautics and Astronautics, Jul. 2024. doi: 10.2514/6.2024-4113.

[11] D. M. Orchard, 'Investigation of tolerance for icing of UAV rotors/propellers: phase 3 test rig development and calibration', National Research Council of Canada. Aerospace. Aerodynamics Laboratory, 2021. doi: 10.4224/40002681.

[12] S. Tarquini, C. Antonini, A. Amirfazli, M. Marengo, and J. Palacios, 'Investigation of ice shedding properties of superhydrophobic coatings on helicopter blades', *Cold Reg Sci Technol*, vol. 100, pp. 50–58, 2014, doi: https://doi.org/10.1016/j.coldregions.2013.12.009.

[13] H. Hu, L. Tian, C. Eluchie, H. Sista, and H. Hu, 'Comparative Study of Using Superhydrophobic and Icephobic Surface Coatings for Aircraft Icing Mitigation', *AIAA Journal*, vol. 62, no. 4, pp. 1588–1600, Apr. 2024, doi: 10.2514/1.J063579/ASSET/IMAGES/LARGE/FIGURE8.JPEG.

[14] E. Villeneuve, A. Samad, C. Volat, M. Beland, and M. Lapalme, 'Experimental Assessment of the Ice Protection Effectiveness of Icephobic Coatings for a Hovering Drone Rotor', *Cold Reg Sci Technol*, 2023, doi: https://doi.org/10.1016/j.coldregions.2023.103858.

[15] R. Fürbacher *et al.*, 'Novel Passive Icephobic Surfaces – Experimental Investigations in a Small-Scale Icing Wind Tunnel', *AIAA Aviation Forum and ASCEND, 2024*, 2024, doi: 10.2514/6.2024-4353.

[16] N. Karpen, S. Diebald, F. Dezitter, and E. Bonaccurso, 'Propeller-integrated airfoil heater system for small multirotor drones in icing environments: Anti-icing feasibility study', *Cold Reg Sci Technol*, vol. 201, p. 103616, 2022, doi: https://doi.org/10.1016/j.coldregions.2022.103616.

[17] N. C. Müller, B. Løw-Hansen, K. T. Borup, and R. Hann, 'UAV icing: Development of an ice protection system for the propeller of a small UAV', *Cold Reg Sci Technol*, vol. 213, p. 103938, Sep. 2023, doi: 10.1016/J.COLDREGIONS.2023.103938.

[18] A. Samad, E. Villeneuve, C. Volat, M. Béland, and M. Lapalme, Experimental Assessment of the Ice Protection Effectiveness of Electrothermal Heating for a Hovering Drone Rotor', *Exp Therm Fluid Sci*, p. 110992, 2023, doi: https://doi.org/10.1016/j.expthermflusci.2023.110992.

[19] A. Samad, A. Dhulipalla, and H. Hu, A Hybrid Anti-/De-icing Strategy for UAV Propeller Icing Protection', *AIAA AVIATION FORUM AND ASCEND 2024*, Jul. 2024, doi: 10.2514/6.2024-4355.

[20] P. H. von Hardenberg, C. A. Flack, and D. L. Rigby, 'Ice Shape Analysis of an eVTOL Propeller in Forward Flight at the NASA Glenn Icing Research Tunnel', *AIAA Aviation Forum and ASCEND, 2024*, 2024, doi: 10.2514/6.2024-4448.

[21] Y. Liu, L. Li, Z. Ning, W. Tian, and H. Hu, 'Experimental investigation on the dynamic icing process over a rotating propeller model', *J Propuls Power*, vol. 34, no. 4, pp. 933–946, 2018, doi: https://doi.org/10.2514/1.B36748.

[22] R. M. Waldman and H. Hu, 'High-speed imaging to quantify transient ice accretion process over an airfoil', *J Aircr*, vol. 53, no. 2, pp. 369–377, Aug. 2016, doi: 10.2514/1.C033367/ASSET/IMAGES/LARGE/FIGURE12.JPEG.

[23] S. E. Campbell, A. P. Broeren, and M. B. Bragg, 'Sensitivity of Aircraft Performance to Icing Parameter Variations', *https://doi.org/10.2514/1.32355*, vol. 44, no. 5, pp. 1758–1760, May 2012, doi: 10.2514/1.32355.

[24] D. Yanxia, G. Yewei, X. Chunhua, and Y. Xian, 'Investigation on heat transfer characteristics of aircraft icing including runback water', *Int J Heat Mass Transf*, vol. 53, no. 19–20, pp. 3702–3707, Sep. 2010, doi: 10.1016/J.IJHEATMASSTRANSFER.2010.04.021.

[25] S. F. Armanini, M. Polak, J. E. Gautrey, A. Lucas, and J. F. Whidborne, 'Decision-making for unmanned aerial vehicle operation in icing conditions', *CEAS Aeronaut J*, vol. 7, no. 4, pp. 663–675, Dec. 2016, doi: 10.1007/S13272-016-0215-2/FIGURES/4.

[26] A. Samad, E. Villeneuve, C. Blackburn, F. Morency, and C. Volat, 'An experimental investigation of the convective heat transfer on a small helicopter rotor with anti-icing and de-icing test setups', *Journal of Aerospace*, vol. 8, no. 4, p. 96, 2021, doi: https://doi.org/10.3390/aerospace8040096.

[27] Z. Bottyán, 'IN-FLIGHT ICING CHARACTERISTICS OF UNMANNED AERIAL VEHICLES DURING SPECIAL ATMOSPHERIC CONDITION OVER THE CARPATHIAN-BASIN', *Acta Geographica Debrecina. Landscape and Environment Series*, 2013.

[28] R. M. Waldman and H. Hu, 'High-Speed Imaging to Quantify Transient Ice Accretion Process over an Airfoil', *https://doi.org/10.2514/1.C033367*, vol. 53, no. 2, pp. 369–377, Aug. 2015, doi: 10.2514/1.C033367.

[29] P. Buchen, D. Sotomayor-Zakharov, and I. Knop, Predicting the Collection Efficiency on a Generic Rotor Blade with a Three-Dimensional Eulerian Particle Solver', Jun. 2023. doi: 10.4271/2023-01-1469.

[30] N. Han, H. Hu, and H. Hu, 'An Experimental Investigation on the Dynamic Ice Accretion Process over the Blade Surface of a Rotating UAV Propeller', in *AIAA SCITECH 2022 Forum*, Reston, Virginia: American Institute of Aeronautics and Astronautics, Jan. 2022. doi: 10.2514/6.2022-1538.

[31] H. Hu, L. Tian, C. Eluchie, H. Sista, and H. Hu, 'An Experimental Study to Compare the Effectiveness of Superhydrophobic Coating and Icephobic Coating for Aircraft Icing Mitigation', Jun. 2023, doi: 10.2514/6.2023-4275.

[32] A. Benmeddour, 'Investigation of tolerance for icing of small UAV rotors/propellers: phase 2', National Research Council of Canada. Aerospace, 2020. doi: 10.4224/40002002.

[33] T. H. Bond and D. N. Anderson, 'Manual of Scaling Methods', Cleveland, Ohio, United States, 2004. [Online]. Available: https://ntrs.nasa.gov/citations/20040042486